Royal Netherlands
Meteorological Institute
Ministry of Infrastructure
and Water Management

TROPOMI ATBD of the Aerosol Optical Thickness

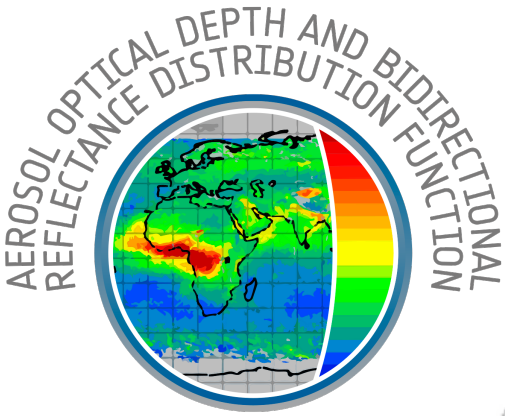

document number	:	S5P-KNMI-L2-0033-RP
authors	:	M. de Graaf
CI identification	:	CI-7430-ATBD
issue	:	4.0.0
date	:	2024-01-31
status	:	released

Document approval record

	digital signature
Prepared:	Martin de Graaf Digitally signed by Martin de Graaf Date: 2024.01.26 17:02:24 +01'00'
Checked:	Gijsbert Tilstra Digitally signed by Gijsbert Tilstra Date: 2024.01.29 10:13:26 +01'00'
Approved PM:	
Approved PI:	

Document change record

issue	date	item	comments
0.0.1	2019-12-12	All	Initial version
0.0.2	2020-03-25	All	Version shared with team (confidential)
0.0.3	2020-06-16	 Sect. 5.3 Sect. 6.3 Sect. 6.8 Sect. 7.4 All	Corrections after review: -Update of quality flags description -Addition of cross section descriptions -Addition of ALH climatology description -Update of Table 8 -Editorial updates
0.1.0	2020-08-25	All	Addition of document number
1.0.0	2020-11-26	All	Release after review
1.0.1	2021-05-26	Ch. 8 and 9	Update of error budget and validation results
2.0.0	2021-06-01	All	Public Release
3.0.0	2022-02-16	All	Update for PAL product implementation, small edits, CI number addition
4.0.0	2024-01-31	Sect. 6.2.4 & Table 5 All Ch. 10	Changed smallest wavelengths to 354 and 388 nm Editorial updates and typo corrections Added PAL reference
		Table. 5	Updated configuration parameters
		Ch. 6.9.3	Added AOT precision
		Table. 8	Synchronized product overview table with L2 product

Contents

List of Tables

List of Figures

1 Introduction

1.1 Identification

This document is identified as S5P-KNMI-L2-0033-RP.

1.2 Purpose and objective

The purpose of this document is to describe the theoretical basis and the implementation of the S5p+I Level-2 products algorithms for TROPOMI. The document was maintained during the development phase of the data products in the context of S5p+I. This is the final of three versions of the document, describing the implementation at the PAL development and production environment.

1.3 Document overview

The document describes the TROPOMI Aerosol Optical Thickness (AOT) algorithm for the L2 product, which will be computed for each cloud-free and sun glint-free TROPOMI pixel.

2 Applicable and reference documents

2.1 Applicable documents

[AD1] TROPOMI Instrument and Performance Overview.
source: KNMI; **ref:** S5p-KNMI-L2-0010-RP; **issue:** 0.10.0; **date:** 2014-03-15.

[AD2] ESA Climate Change Initiative, Option 3 Absorbing Aerosol Round Robin.
source: ESA; **ref:** Aerosol Absorption; **issue:** 1.2; **date:** 2018-03-15.

[AD3] TROPOMI ATBD of the directionally dependent surface Lambertian-equivalent reflectivity.
source: KNMI; **ref:** S5P-KNMI-L2-0033-RP; **issue:** 1.0.0; **date:** 2021-06-01.

[AD4] OMI Algorithm Theoretical Basis Document - Volume III - Clouds, Aerosol, and Surface UV Irradiance.
source: KNMI; **ref:** ATBD-OMI-03; **issue:** 2.0; **date:** 2002-08.

[AD5] TROPOMI validation report of the Aerosol Optical Thickness product.
source: KNMI; **ref:** S5P-KNMI-L2-0402-RP; **issue:** 1.0.0; **date:** 2021-06-01.

2.2 Standard documents

[SD1] Space Engineering – Software.
source: ESA/ECSS; **ref:** ECSS-E-ST-40C; **date:** 2009-03-06.

2.3 Reference documents

[RD1] Terms and symbols in the TROPOMI Algorithm Team.
source: KNMI; **ref:** S5P-KNMI-L2-0049-MA; **issue:** 1.0.0; **date:** 2015-07-16.

[RD2] H. Jethva and O. Torres; Satellite-based evidence of wavelength-dependent aerosol absorption in biomass burning smoke inferred from Ozone Monitoring Instrument. *Atmos. Chem. Phys.*; **11** (2011), 10541; 10.5194/acp-11-10541-2011.

[RD3] B. T. Johnson, K. P. Shine and P. M. Forster; The semi–direct aerosol effect: Impact of absorbing aerosols on marine stratocumulus. *Quart. J. Roy. Meteor. Soc.*; **130** (2004), 1407; 10.1256/qj.03.61.

[RD4] M. de Graaf, N. Bellouin, L. G. Tilstra *et al.*; Aerosol direct radiative effect of smoke over clouds over the southeast Atlantic Ocean from 2006 to 2009. *Geophys. Res. Lett.*; (2014); 10.1002/2014GL061103. URL http://dx.doi.org/10.1002/2014GL061103.

[RD5] Omar Torres, Hiren Jethva and P. K. Bhartia; Retrieval of Aerosol Optical Depth above Clouds from OMI Observations: Sensitivity Analysis and Case Studies. *J. Atmos. Sci.*; **69** (2011) (3), 0022–4928; 10.1175/JAS-D-11-0130.1.

[RD6] Hiren Jethva, Omar Torres, Fabien Waquet *et al.*; How do A-train Sensors Intercompare in the Retrieval of Above-Cloud Aerosol Optical Depth? A Case Study-based Assessment. *Geophys. Res. Lett.*; **41** (2014); 10.1002/2013GL058405.

[RD7] F. Peers, P. Francis, C. Fox *et al.*; Observation of absorbing aerosols above clouds over the south-east Atlantic Ocean from the geostationary satellite SEVIRI – Part 1: Method description and sensitivity. *Atmos. Chem. Phys.*; **19** (2019) (14), 9595; 10.5194/acp-19-9595-2019.

[RD8] O. Torres, P. K. Bhartia, J. R. Herman *et al.*; A Long-Term Record of Aerosol Optical Depth from TOMS Observations and Comparison to AERONET Measurements. *J. Atmos. Sci.*; **59** (2002) (3), 398; 10.1175/1520-0469.

[RD9] O. Torres, A. Tanskanen, B. Veihelmann *et al.*; Aerosols and surface UV products from Ozone Monitoring Instrument observations: An overview. *J. Geophys. Res.*; **112** (2007), D24S47; 10.1029/2007JD008809.

[RD10] O. Torres, C. Ahn and Z. Chen; Improvements to the OMI near-UV aerosol algorithm using A-train CALIOP and AIRS observations. *Atmos. Meas. Tech.*; **6** (2013) (11), 3257; 10.5194/amt-6-3257-2013.

[RD11] N. Schutgens, O. Dubovik, O. Hasekamp *et al.*; AEROCOM and AEROSAT AAOD and SSA study – Part 1: Evaluation and intercomparison of satellite measurements. *Atmos. Chem. Phys.*; **21** (2021) (9), 6895; 10.5194/acp-21-6895-2021. URL https://acp.copernicus.org/articles/21/6895/2021/.

[RD12] O. Dubovik, M. Herman, A. Holdak *et al.*; Statistically optimized inversion algorithm for enhanced retrieval of aerosol properties from spectral multi-angle polarimetric satellite observations. *Atmospheric Measurement Techniques*; **4** (2011) (5), 975; 10.5194/amt-4-975-2011.

[RD13] John H. Seinfeld and Spyros N. Pandis; *Atmospheric Chemistry and Physics: From Air Pollution to Climate Change* (Whiley, 2016); ISBN 978-1-118-94740-1.

[RD14] K. N. Liou; *An Introduction to Atmospheric Radiation* (Academic Press, 2002).

[RD15] L. V. Lorenz; Lysbevaegelsen i og uder en plane lysbolger belyst kulge. *Vidensk. Selk. Skr.*; **6** (1890), 1.

[RD16] G. Mie; Beiträge zur Optik trüber Medien, speziell kolloidaler Metallösungen. *Ann. Phys. Leipzig*; **25** (1908), 377.

[RD17] J. Heintzenberg and R. M. Welch; Retrieval of aerosol size distribution from angular scattering functions: effects of particle composition and shape. *Appl. Opt.*; **21** (1982) (5), 822; 10.1364/AO.21.000822. URL http://ao.osa.org/abstract.cfm?URI=ao-21-5-822.

[RD18] J. F. De Haan, P. B. Bosma and J. W. Hovenier; The adding method for multiple scattering calculations of polarized light. *Astron. & Astrophys.*; **183** (1987), 371.

[RD19] D. Daumont, J. Brion, J. Charbonnier *et al.*; Ozone UV spectroscopy I: Absorption cross-sections at room temperature. *J. Atmos. Chem.*; **15** (1992), 145; 10.1007/BF00053756.

[RD20] J. Malicet, D. Daumont, J. Charbonnier *et al.*; Ozone UV spectroscopy. II. Absorption cross-sections and temperature dependence. *J. Atmos. Chem.*; **21** (1995), 263; 10.1007/BF00053756.

[RD21] A. C. Vandaele, C. Hermans, P. C. Simon *et al.*; Measurements of the NO_2 absorption cross-section from 42,000 cm^{-1} to 10,000 cm^{-1} (238-1000 nm) at 220 K and 294 K. *J.Q.S.R.T*; **59** (1998) (3-5), 171; 10.1016/S0022-4073(97)00168-4.

[RD22] S. Chandrasekhar; *Radiative Transfer* (Dover, Mineola, N.Y., 1960).

[RD23] Charles Cox and Walter Munk; Measurement of the Roughness of the Sea Surface from Photographs of the Sun's Glitter. *J. Opt. Soc. Am.*; **44** (1954) (11), 838; 10.1364/JOSA.44.000838. URL http://www.osapublishing.org/abstract.cfm?URI=josa-44-11-838.

[RD24] A. Bozzo, A. Benedetti, J. Flemming *et al.*; An aerosol climatology for global models based on the tropospheric aerosol scheme in the Integrated Forecasting System of ECMWF. *Geosci. Model Dev.*; **13** (2020) (3), 1007; 10.5194/gmd-13-1007-2020. URL https://www.geosci-model-dev.net/13/1007/2020/.

[RD25] O. Torres, P. K. Bhartia, J. R. Herman *et al.*; Derivation of aerosol properties from satellite measurements of backscattered ultraviolet radiation: Theoretical basis. *J. Geophys. Res.*; **103** (1998), D14; 10.1029/98JD00900.

2.4 Electronic references

[ER1] URL http://spectrolab.aeronomie.be.

[ER2] URL https://data-portal.s5p-pal.com.

3 References, terms and acronyms

Terms, definitions and abbreviated terms for TROPOMI Level 2 algorithms are described in [RD1]. Abbreviation specific for this document are defined below.

3.1 Terms, definitions and abbreviated terms

AAI	Absorbing Aerosol Index
AAOT	Aerosol Absorption Optical Thickness
AOD	Aerosol Optical (Penetration) Depth
AOT	Aerosol Optical Thickness (partial - layer, or total - atmosphere)
ATBD	Algorithm Theoretical Baseline Document
BRDF	Bidirectional Reflectance Distribution Function
BSA	Black-Sky Albedo
CAMS	Copernicus Atmosphere Monitoring Service
CF	Climate and Forecast metadata conventions
DAK	Doubling-Adding KNMI
DU	Dobson Units, 2.69×10^{16} molecules cm^{-2}
ECMWF	European Centre for Medium-Range Weather Forecast
ENVISAT	Environmental Satellite
EOS-Aura	Earth Observing System – Aura satellite
EPS-SG	EUMETSAT Polar System – Second Generation
ERS	European Remote Sensing Satellite
ESA	European Space Agency
EUMETSAT	European Organisation for the Exploitation of Meteorological Satellites
FOV	Field-of-View
FRESCO	Fast Retrieval Scheme for Clouds from the Oxygen A band
GMTED2010	Global Multi-resolution Terrain Elevation Data 2010
GOME	Global Ozone Monitoring Experiment
HDF	Hierarchical Data Format
KNMI	Koninklijk Nederlands Meteorologisch Instituut
LER	Lambertian-Equivalent Reflectivity
LUT	Look-Up Table
L2OP	Level-2 Operational Processor
L2PP	Level-2 Prototype Processor
MERIS	Medium Resolution Imaging Spectrometer
METOP	Meteorological Operational Satellite
MLS	Mid-Latitude Summer
NASA	National Aeronautics and Space Administration
NISE	Near-real-time Ice and Snow Extent
NRT	Near-Real-Time
OMI	Ozone Monitoring Instrument
PAL	Product Algorithm Laboratory
PAM	Performance Assessment Module
RAA	Relative Azimuth Angle
RMSE	Root-Mean-Square Error
RTM	Radiative Transfer Model
SAA	Solar Azimuth Angle
SCIAMACHY	Scanning Imaging Absorption Spectrometer for Atmospheric Chartography

SW	Software
SZA	Solar Zenith Angle
S5	Sentinel-5 mission
S5P	Sentinel-5 Precursor mission
Suomi-NPP	Suomi-National Polar-Orbiting Partnership
TOA	Top-of-Atmosphere
TOMS	Total Ozone Mapping Spectrometer
TROPOMI	Tropospheric Monitoring Instrument
UTC	Coordinated Universal Time
UV	Ultraviolet
UVNS	Ultraviolet Visible Near-infrared Shortwave spectrometer
VAA	Viewing Azimuth Angle
VIS	Visible
VZA	Viewing Zenith Angle

4 TROPOMI Instrument description

A description of the TROPOMI instrument and performance can be found in [AD1].

5 Introduction to the TROPOMI AOT product

Aerosol particles scatter and absorb light, thus affecting the radiation field in the atmosphere. On the short-term, this may have impact on weather, and over longer term on climate. In addition to direct radiative effects due to scattering and absorption, aerosols also impact the formation, the droplet size, the albedo, precipitation and lifetime of clouds. These aerosol-cloud interactions thus also impact weather and climate. Additionally, aerosols have adverse health effects. Especially small aerosol particles can penetrate deep into the respiration system, causing short-term and long-term health risks. Depending on the application, aerosols can be classified in different ways.

- A common classification for aerosol is according to their sources. Aerosol particles which are emitted as particles, such as desert dust, volcanic ash or sea salt, are referred to as primary aerosols. Secondary aerosols are formed within the atmosphere from precursor gases, such as sulfur dioxide, nitrogen dioxide, organics and ammonia. Due to their different formation process, primary aerosol particles are generally larger than secondary aerosol particles.
- Another way of classifying aerosol particles is according to their radiation absorption. The amount of absorption is commonly expressed as the single scattering albedo, which is defined as the ratio between scattering and extinction. The single scattering albedo of atmospheric aerosols varies in the range between approximately 0.7 and 1.0. Absorbing components in aerosol particles that determine the amount of absorption include iron oxides in desert dust and volcanic plumes, and black and brown carbon for plumes resulting from (incomplete) combustion processes.
- A third classification of aerosol particles is according to their hygroscopic behaviour. Aerosol particles that contain a significant amount of chemical components that will attract water when the relative humidity increases, such as sea salt, ammonium sulfate and ammonium nitrate, as well as sulfuric acid, are called hygroscopic. Hygroscopic particles will significantly change size and composition with changing relative humidity, which also impacts their scattering and absorbing properties. Particles that do not attract water are called hydrophobic.
- Finally, aerosol particles are also classified according to their shape. Primary particles that are hydrophobic, such as desert dust and volcanic ash, are generally non-spherical. Secondary aerosols and hygroscopic particles are generally spherical.

The algorithm described in this document is designed to retrieve the aerosol optical thickness (AOT) in the wavelength range between 354 and 494 nm. This wavelength range is selected because it contains unique information on absorption by aerosols. The high-spectral information from UVNS spectrometers like TROPOMI is important to derive the spectral variation in aerosol absorption, and should be exploited as such. There are indications that the absorption by aerosols in the UV may be much larger than previously anticipated [RD2], and the UV-absorption has important consequences for the formation and life-time of clouds [RD3, RD4]. It is expected the 3MI instrument on Metop Second Generation, which is designed to derive aerosol properties, will provide the AOT in the visible and near-infrared with a higher trueness and spatial resolution than what can be achieved from the UVNS instrument.

5.1 Heritage

Satellite observations in the wavelength region from approximately 340 to 400 nm are sensitive to the presence of elevated absorbing aerosols. The UV Aerosol Index (UVAI, also called absorbing aerosol index or AAI) has been derived from almost all ozone monitoring instruments such as TOMS, GOME-1, SCIAMACHY, OMI and GOME-2. Although the UVAI is widely used, it also has its limitations. The main limitation is that the UVAI is not a geophysical quantity, and as such it cannot be compared to models or observations using other techniques. Therefore, this ATBD focuses on the AOT and the absorbing part of the AOT (AAOT). The AOT and AAOT can only be derived for cloud-free pixels, because the algorithm cannot distinguish between clouds and aerosols. In addition, it is not possible to derive AOT and AAOT over strongly reflecting surfaces such as snow or ice. This is an important limitation of the product. Note that the retrieval of AOT and AAOT over clouds is a field of active research [RD5, RD4, RD6, RD7].

Since cloud contamination is one of the largest challenges for AOT retrievals from satellite observations and the number of cloud-free pixels depends strongly on the spatial resolution of the observations, satellite instruments designed to detect aerosols, such as MODIS, MISR and 3MI, have a relatively high spatial

resolution and a relatively low spectral resolution. On the other hand, satellite instruments that have been designed to observe the 340 to 400 nm range to measure trace gases, traditionally have a high spectral resolution but a low spatial resolution. OMI with 13x24 km^2 had the best spatial resolution in the targeted wavelength region. For OMI, two AOT products were developed: the OMAERO algorithm that uses 14 wavelengths in the range 354 – 500 nm, and the OMAERUV algorithm that is based on the retrieval at 354 and 388 nm [RD8, RD9, RD10]. The OMAERUV algorithm is especially targeting the wavelength range that is also the main target for this ATBD and has been designed to derive both the AOT and AAOT (through SSA). Both the OMAERO and the OMAERUV algorithms are using a look-up table (LUT) approach. The algorithm described in this ATBD for S5P/TROPOMI combines these approaches. At a spatial resolution of TROPOMI of 5.5x3.5 km^2 and spectral resolution of 0.2 nm the AOT product has similar accuracy as traditional satellite AOT products.

The combination of AOT and AAOT is especially important to distinguish different aerosol types, e.g. desert dust, biomass burning and weakly absorbing particles. In addition, it is directly related to the absorption of solar radiation in aerosol layers, which affect the radiation balance and vertical stability of the atmosphere, and modify the formation processes and the lifetime of clouds. Note however, that the AAOT product is not expected to be very accurate for a single view instrument like TROPOMI. More information should be combined for a more accurate retrieval of intrinsic aerosol properties [AD2]. However, with a suitable mathematical treatment, AAOT and SSA can still be useful for the evaluation of model AOT [RD11].

In addition to the specialized TROPOMI algorithm, a generalized aerosol retrieval algorithm GRASP was developed in parallel [RD12]. The GRASP algorithm can handle the UV wavelength range and is an iterative scheme, based on on-line radiative transfer. The GRASP is a prime example of an algorithm that combines as much information as possible to retrieve aerosol and surface characteristics.

AOT at visible and NIR wavelength are also available, e.g. from the specialised instruments like MODIS, MISR and 3MI. An effective AOT at 760 nm is available from the S5P ALH algorithm, which fits the reflectance spectrum in the O_2-A band in the NIR wavelength band. However, the aerosol model for this fit is a very simple one.

5.2 Requirements

These are the GCOS climate application requirements for AOT:

- The uncertainty in the aerosol optical thickness (AOT) for two or more wavelengths in the spectral region between 340 nm and 390 nm shall be smaller than 0.05 (target) to 0.10 (threshold) or 10% (target) to 25% (threshold). Depending on the scenario the least stringent of the absolute and the relative requirements applies.
- The uncertainty in the aerosol optical thickness (AOT) for one or more wavelengths in the spectral region between 390 nm and 500 nm shall be smaller than 0.02 (target) to 0.10 (threshold) or 10(target) to 25% (threshold). Depending on the scenario the least stringent of the absolute and the relative requirements applies.

The S5P-TROPOMI AOT and AAOT at the UV wavelengths are not expected to meet these requirements. Based on the experience with the OMAERUV algorithm and expected improvements of the algorithm and the instrument, an accuracy of 0.1 or 25% (whichever is largest) is expected for near-global, operational performance (solar zenith angles less than 70°). Larger errors are expected for high solar zenith angles. At higher solar zenith angles the problems with cloud clearing will increase due to the longer path through the atmosphere. Also, the representation errors between the satellite and the ground-based observation will increase. Furthermore, uncertainties in the radiative transfer will become larger. Therefore the performance range to solar zenith angles is limited to less than 70°. At higher solar zenith angles the data will be flagged as having lower quality.

5.3 Quality assurance

In order to report the quality of individual pixels, quality flags are available on pixel level, which can be raised to indicate lower than optimal quality. An example is the flag indicating a solar zenith angle larger than 70°. Several flags are available, given in table 1. The configuration values in table 1 are specified in table 5.

Flag	Description
Solar zenith angle flag	Solar zenith angle $>$ SZA_0
Cloud fraction flag	Cloud fraction between CF_max1 and CF_max1
sun glint flag	Sun glint angle $<$ Θ_SG_1

Table 1: Quality flags

5.4 Processor version

The decription in this ATBD refers to processor version 2.0.0.

6 Algorithm description

6.1 Light scattering and absorption

A pencil of radiation, with wavelength λ, traversing an extinction medium, will be attenuated by its interaction with the medium. The intensity of the radiation after traversing a thin slice of the medium, of thickness dz, will be reduced by $\mathrm{d}I = -\sigma(z)I\mathrm{d}z$, where σ is the attenuation coefficient of the medium. If I_0 is the incident radiation intensity, the emergent intensity at a distance z can be found by integration to be $I(\lambda,z) = I_0(\lambda)e^{-\tau}$, where τ is the medium optical depth. This solution is known as the Bouguer-Lambert-Beer law. If the extinction medium is the Earth's atmosphere, the optical penetration depth (AOD) $\tau(\lambda,z)$ can be described as

$$\tau(\lambda,z) = \int_z^{\infty} \sigma_{\mathrm{ext}}^{\mathrm{atm}}(\lambda,z')\,\mathrm{d}z', \tag{1}$$

where the integration is from the top of the atmosphere to an altitude z in the atmosphere, and $\sigma_{\mathrm{ext}}^{\mathrm{atm}}$ is the atmospheric extinction coefficient, which describes the attenuation of the light beam due to scattering and absorption in the atmosphere, and is the sum of the scattering coefficient $\sigma_{\mathrm{sca}}^{\mathrm{atm}}$ and the absorption coefficient $\sigma_{\mathrm{abs}}^{\mathrm{atm}}$, in units of [m^{-1}],

$$\sigma_{\mathrm{ext}}^{\mathrm{atm}} = \sigma_{\mathrm{sca}}^{\mathrm{atm}} + \sigma_{\mathrm{abs}}^{\mathrm{atm}}. \tag{2}$$

The extinction coefficient is dependent on the refractive index of the material. In the Earth's atmosphere it is convenient to separate the extinction by gases, clouds and by aerosols. In the algorithm, the extinction due to aerosols alone is considered, by computing the extinction due to (gas) molecules (which is relatively straightforward since the atmospheric gaseous composition is well-known and well-computable) and applying the algorithm to cloud-free scenes only.

6.2 Light scattering and absorption by aerosols in the atmosphere

6.2.1 Aerosol (absorption) optical thickness

The total aerosol optical thickness (AOT) of the atmosphere can be obtained by substituting the aerosol extinction coefficient σ_{ext} in equation 1 and integrating from the surface to the top of the atmosphere:

$$AOT(\lambda) = \int_0^{\infty} \sigma_{\mathrm{ext}}(\lambda,z)\,\mathrm{d}z. \tag{3}$$

The absorption aerosol optical thickness (AAOT) of the atmosphere, which describes the total absorption of the light by aerosols in the atmosphere, can be expressed as

$$AAOT(\lambda) = \int_0^{\infty} (1-\omega_0(\lambda,z))\sigma_{\mathrm{ext}}(\lambda,z)\,\mathrm{d}z, \tag{4}$$

where $\omega_0 = \sigma_{\mathrm{sca}}/\sigma_{\mathrm{ext}}$ is the single scattering albedo, defining the fraction of scattering and absorption of radiation in the atmosphere. This is generally determined by the refractive index of the particles m, which is an imaginary number $m = m_r - \boldsymbol{i}m_i$.

If the extinction medium considered consists of many scattering and absorbing particles, the aerosols extinction coefficient σ_{ext} is the product of the extinction cross section C_e of the particles [m^2] and the number density n [m^{-3}],$\sigma_{\mathrm{ext}} = C_e \cdot n(r)$. The number density is size dependent, and the total number of particles with radii between r_1 and r_2 is given by

$$N(r_1;r_2) = \int_{r_1}^{r_2} \frac{dN(r)}{dr} dr. \tag{5}$$

6.2.2 Size distribution functions for atmospheric aerosols

Atmospheric aerosol size distributions can often be approximated by a bi-modal log-normal size distribution [RD13], defined by

$$\frac{dN}{d\ln r} = (1-w^{\mathrm{f}})\cdot \mathrm{L}^{\mathrm{c}} + (w^{\mathrm{c}})\cdot \mathrm{L}^{\mathrm{c}}, \tag{6}$$

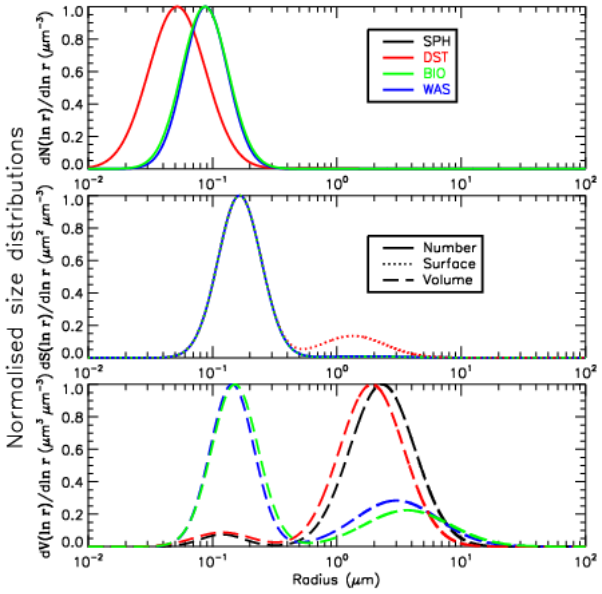

Figure 1: Normalised number, surface, and volume size distributions for the BIO, WAS, and DST models, and volume size distribution for the SPH model.

where r is particle radius, L^f and L^c are the log-normal distributions of a fine mode part of the particles and a coarse mode part of the particles, respectively. The log-normal distribution is defined as

$$L(\ln r) = \frac{N}{\sqrt{2\pi}\ln(v_g)} \exp\left(-\frac{(\ln r - \ln r_g)^2}{2\ln^2 v_g}\right), \tag{7}$$

where r_g is the median radius of the particles and v_g the geometric standard deviation, describing the width of the distribution. Alternatively, the volume size distribution can be specified as

$$L(\ln V) = \frac{N}{\sqrt{2\pi}\sigma_g} \exp\left(-\frac{(\ln V - \sigma_g)^2}{2\sigma_g^2}\right). \tag{8}$$

Example bi-modal size number, surface and volume size distribution functions are illustrated in Figure 1 for various aerosol models used in the algorithm. The exact definitions of the size distribution parameters are defined below.

6.2.3 Light scattering by atmospheric aerosols

The distribution of the scattered light intensity I as a function of scattering angle Θ at a distance R from the scatterer is generally expressed in terms of the phase function $P_{11}(\Theta)$:

$$I(\Theta) = I_0 \frac{\sigma_{sca}}{R^2} \frac{P_{11}(\Theta)}{4\pi}, \tag{9}$$

where P_{11} is the first component of the 4x4 scattering matrix $\mathbf{P}$, which describes the distribution of incoming polarized light $\mathbf{I}^0$ due to the interaction with atmospheric aerosols:

$$\mathbf{I} = \mathbf{P}\,\mathbf{I}^0 \tag{10}$$

Here, the polarized light beam is described by a set of four *Stokes parameters* (e.g. [RD14]), $\mathbf{I} = [I, Q, U, V]^T$, describing the intensity I, linear polarization Q and U, and vertical polarization V of the light beam.

The scattering phase function P_{11} is given for different scatterers in the left panel of Figure 2. The scattering by scatterers that have a radius r that is much smaller than the wavelength λ of the scattered light ($2\pi r < \lambda$), which is true for e.g. molecules, is termed Rayleigh scattering, and is equal in the forward and backward direction. This is shown by the solid line with filled circles in Figure 2. The light intensity scattering angles

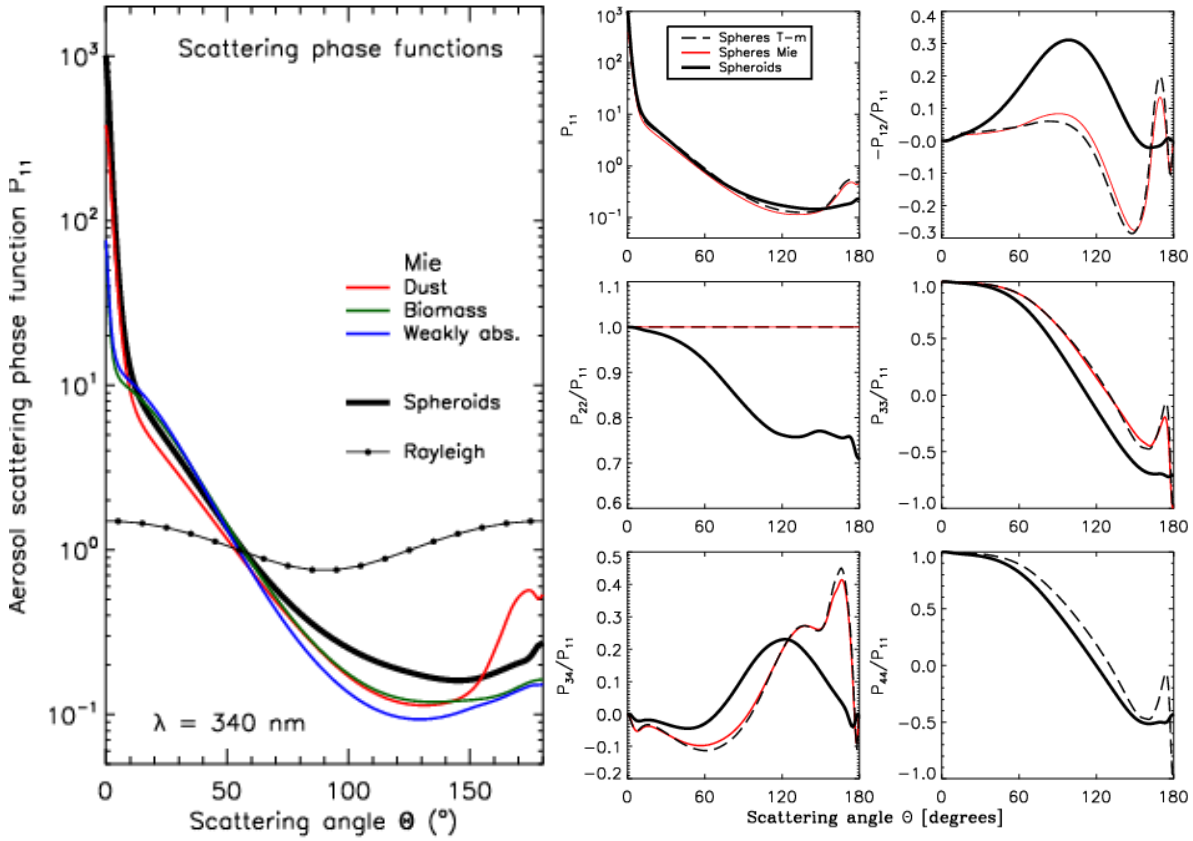

Figure 2: (left) Phase functions for different aerosol models and molecules. Dashed lines: Mie 'dust', 'biomass burning' and 'weakly absorbing' aerosol models. Fat solid line: Spheroidal dust aerosol model. Thin solid line: Molecular scattering phase function. (right) Dust model scattering phase matrix elements, normalised to the first element, computed using different methods. In red and blue the scattering phase matrix elements are compared for spheres computed with the T-matrix method (red) using the bimodal lognormal volume size distribution function given in Table 2 and the Mie method (blue) using a bimodal lognormal number size distribution as given in Table 2. The scattering phase matrix elements for the spheroidal aerosol model is given in green.

and extinction and scattering coefficients for isotropic homogeneous spherical particles which are larger than the wavelength λ of visible light ($2\pi r > \lambda$) can be computed using Lorenz-Mie theory [RD15, RD16]. The phase functions of several different spherical particle models are shown in Figure 2 by the colored lines. The scattering by large suspended particles is orders of magnitudes larger in the forward direction than in the backward direction.

A spherical aerosol shape introduces peaks in the scattering phase function, especially in the backscatter direction and at side scattering angles, which is often not found in the scattering distribution of real atmospheric aerosols. Hygroscopic aerosols can be reasonably assumed to be spherical as they are quickly coated by water, but this is often not the case for desert dust, for which strongly non-spherical shapes are found [RD17]. For an accurate retrieval of particle properties of dust, it is important to remove the peaks in the scattering phase matrices that are a result of the symmetries in a sphere. To account for the non-sphericity, a spheroidal shape is assumed for dust, which is one of the simplest deviation from the symmetric sphere form. A spheroid can be created by rotating an ellipse about one of its principle axes. Rotation about its major axis creates a prolate spheroid, while rotation about its minor axis results in a oblate spheroid. Different forms are possible by elongating the main axis of an ellipse. In the LUT the dust aerosols are represented by a collection of randomly oriented spheroids ranging from oblate to prolate shapes. This effectively smooths the scattering phase function.

The effect of the spheroidal model is illustrated in the right panel Figure 2, which compares the scattering phase matrix elements for dust, computed in three different ways: using Lorenz-Mie theory (red), using T-matrix

theory applied to spheres (black dashed line) and T-matrix theory applied to spheroids (black fat line). The small differences between the spherical phase matrix elements from Lorenz-Mie and T-matrix computations are due to slightly different size distributions. The Lorenz-Mie dust model is specified using the number size distribution parameters given in Table 2, while the T-matrix dust models are specified using the volume size distribution parameters in the same table. The size distributions are plotted in Figure 1. It shows the normalised number, surface, and volume size distributions for the Mie models, and the volume size distribution of the spheroidal model. The volume size distributions of the spherical and spheroidal dust models are slightly different. Note that the Lorenz-Mie dust model is only presented for comparison. In the LUT the spheroidal model is used, which can clearly give large differences with the spherical model.

6.2.4 Aerosol models

In the algorithm, three types of aerosol models are defined, which are all subdivided into seven subtypes, each with their unique scattering and absorption parameters and size distribution functions. The main types represent typical 'desert dust' aerosols, 'biomass burning' aerosols and 'weakly absorbing' aerosols. Seven subtypes were defined, representing increasing absorption for each main type, resulting in 21 distinct aerosol models. The refractive index and size distribution parameters for all 21 aerosols models are given in Table 2. For the 'desert dust' type, the scattering phase function was modeled using spheroids, for the other two main types spherical shapes were assumed.

In Table 2 the number size distribution parameters are also given for a spherical dust model, to illustrate the differences with the spheroidal model.

In Figure 3 the effect of the spheroidal shape distribution is shown. In the left panel the LUT nodes for the spherical model are plotted, while in the right plot the nodes for the spheroidal model are plotted. A retrieval, depicted as the red star, will result in a different absorption coefficient and (A)AOT for the spherical model

Table 2: Complex refractive index and size distribution parameters for the three spherical aerosol types and the spheroidal model and their seven subtypes.

aerosol model	subtype	m_i at λ (nm) nodes					bi-modal size distribution parameters				
		354	388	416	440	494	r_g^f	v_g^f	r_g^c	v_g^c	w^c
biomass burning aerosol spheres m_r=1.5	1	0.00000	0.00000	0.00000	0.00000	0.00000	0.087	1.537	0.567	2.203	$2.06{\cdot}10^{-4}$
	2	0.00600	0.00548	0.00505	0.00469	0.00386	0.087	1.537	0.567	2.203	$2.06{\cdot}10^{-4}$
	3	0.01200	0.01096	0.01011	0.00937	0.00771	0.087	1.537	0.567	2.203	$2.06{\cdot}10^{-4}$
	4	0.02400	0.02192	0.02020	0.01873	0.01543	0.08	1.492	0.705	2.075	$2.05{\cdot}10^{-4}$
	5	0.03600	0.03288	0.00303	0.02810	0.02314	0.08	1.492	0.705	2.075	$2.05{\cdot}10^{-4}$
	6	0.04800	0.04384	0.04041	0.03747	0.03086	0.08	1.492	0.705	2.075	$2.05{\cdot}10^{-4}$
	7	0.05760	0.05260	0.04849	0.04496	0.03703	0.08	1.492	0.705	2.075	$2.05{\cdot}10^{-4}$
weakly absorbing aerosols spheres m_r=1.4	1	0.0000	0.0000	0.0000	0.0000	0.0000	0.088	1.499	0.509	2.160	$4.04{\cdot}10^{-4}$
	2	0.0020	0.0020	0.0020	0.0020	0.0020	0.088	1.499	0.509	2.160	$4.04{\cdot}10^{-4}$
	3	0.0040	0.0040	0.0040	0.0040	0.0040	0.088	1.499	0.509	2.160	$4.04{\cdot}10^{-4}$
	4	0.0060	0.0060	0.0060	0.0060	0.0060	0.088	1.499	0.509	2.160	$4.04{\cdot}10^{-4}$
	5	0.0080	0.0080	0.0080	0.0080	0.0080	0.088	1.499	0.509	2.160	$4.04{\cdot}10^{-4}$
	6	0.0100	0.0100	0.0100	0.0100	0.0100	0.088	1.499	0.509	2.160	$4.04{\cdot}10^{-4}$
	7	0.0120	0.0120	0.0120	0.0120	0.0120	0.088	1.499	0.509	2.160	$4.04{\cdot}10^{-4}$
dust spheres		like spheroids					0.052	1.697	0.670	1.806	$4.35{\cdot}10^{-3}$
							V_g^f	σ_g^f	V_g^c	σ_g^c	w^c
dust aerosol **spheroids** m_r=1.56	1	0.00000	0.00000	0.00000	0.00000	0.00000	0.052	0.4	2.320	0.6	$9.532{\cdot}10^{-3}$
	2	0.00128	0.00117	0.00108	0.00100	0.00082	0.052	0.4	2.320	0.6	$9.532{\cdot}10^{-3}$
	3	0.00256	0.00234	0.00215	0.00199	0.00164	0.052	0.4	2.320	0.6	$9.532{\cdot}10^{-3}$
	4	0.00561	0.00512	0.00472	0.00437	0.00359	0.052	0.4	2.320	0.6	$9.532{\cdot}10^{-3}$
	5	0.00832	0.00760	0.00700	0.00648	0.00532	0.052	0.4	2.320	0.6	$9.532{\cdot}10^{-3}$
	6	0.01279	0.01168	0.01076	0.00997	0.00818	0.052	0.4	2.320	0.6	$9.532{\cdot}10^{-3}$
	7	0.02303	0.02103	0.01937	0.01794	0.01473	0.052	0.4	2.320	0.6	$9.532{\cdot}10^{-3}$

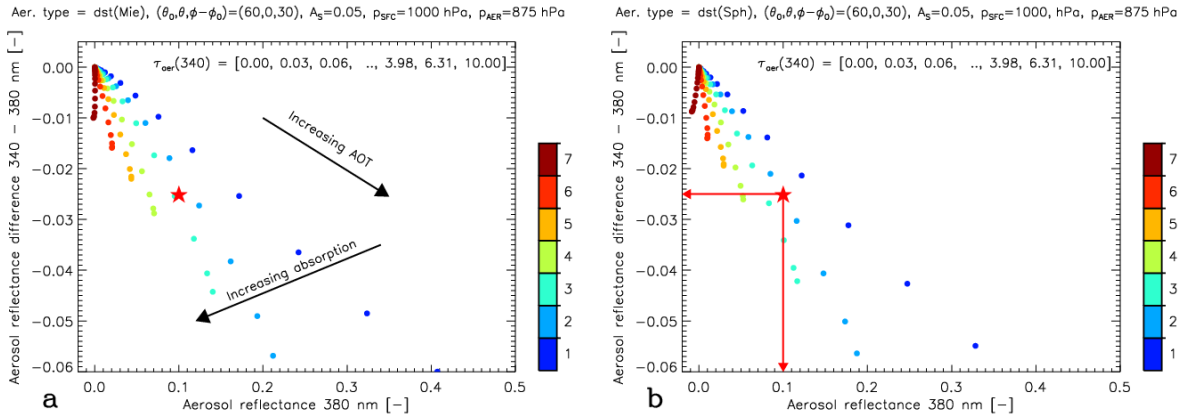

Figure 3: (a) Example of a LUT retrieval (indicated by the red star) using the spherical DST model. The aerosol reflectance vs. difference in aerosol reflectance at 354 and 388 nm is uniquely defined and the measurements at these wavelengths can be used to retrieve the AOT; (b) Same as (a) but for the spheroidal SPH model. The example retrieval shows that a different shape parameterisation can result in different aerosol characterisation. In this case DST type 3 is selected, while SPH type 2 is selected, resulting in a different aerosol AAOT and SSA for the same measurement.

compared to the spheroidal model.

For each of the 21 aerosol models, model atmosphere reflectance lookup tables (LUT) were created to simulate the reflectance measured at the top-of-atmosphere (TOA), as seen by a satellite instrument, described next.

6.3 RTM Lookup Table

The look-up tables (LUTs) were created using the radiative transfer code 'Doubling- Adding KNMI' (DAK) [RD18]. This vector radiative transfer model (RTM) takes polarisation into account, as well as absorption by various trace gases and Lambertian surface reflection. The DAK simulations basically represent a homogeneous clear-sky Rayleigh scattering atmosphere which is bounded below by a Lambertian surface. We used version 3.2.0 of the DAK RTM. This version supports pseudo-spherical treatment of the Earth's atmosphere. Absorption by ozone (cross sections from [RD19] and [RD20]), NO2 (cross sections from [RD21]) and by the O2–O2 collision complex [ER1] is included in the radiative transfer calculations. The wavelength bands for AOT are chosen in such a way that there is little to no absorption by trace gases, allowing monochromatic calculations. This also avoids the need for a slit function of the TROPOMI instrument.

DAK simulates the Earth reflectance, which is defined in the usual way in this ATBD as

$$R = \frac{\pi I}{\mu_0 E_0}, \tag{11}$$

where I is the Earth radiance reflected by the Earth atmosphere and surface, E_0 is the solar irradiance at TOA perpendicular to the direction of the incident sunlight and μ_0 is the cosine of the solar zenith angle θ_0. So $\mu_0 E_0$ is the solar irradiance at TOA incident on a horizontal surface unit. For Lambertian surface reflection, which reflects incident radiation uniformly and unpolarized in all directions, the surface contribution to the reflectance at TOA can be separated from that of the atmosphere [RD22],

$$R(\lambda,\mu,\mu_0,\phi-\phi_0,A_s) = R_0(\lambda,\mu,\mu_0,\phi-\phi_0) + \frac{A_s^{\text{diff}} T(\lambda)}{1-A_s^{\text{diff}} s^*(\lambda)} + \left(A_s^{\text{dir}} - A_s^{\text{diff}}\right)\cdot\exp(-(1/\mu_0+1/\mu)\cdot\tau_{tot}). \tag{12}$$

The first term, R_0, is the path radiance, which is the atmospheric contribution to the reflectance, depending on the relative azimuth angle $\phi-\phi_0$. The second term is the azimuth-independent contribution of the surface with an albedo A_s. Here, $T = t(\mu)t(\mu_0)$, where t is the total atmospheric transmission, dependent on μ_0 and μ, which is the cosine of the viewing zenith angle θ and s^* is the spherical albedo of the atmosphere for illumination from below. The third term is the direct component of the surface contribution A_s^{dir} to the TOA

reflectance, where τ_{tot} is the total optical thickness of the atmosphere. It is an approximation to the specular reflectance of the ocean surface. Over land, $A_s^{\mathrm{dir}} = A_s^{\mathrm{diff}}$ and the third term disappears.

The path radiance and surface albedo can be calculated using tabulated values of $a_i(\mu, \mu_0)$, $t(\mu)$ and s^* for all wavelengths used. Therefore, Lookup tables of a_i, $t(\mu)$ and s^* were prepared, with dimensions as listed in Table 3 and for all parameters listed in Table 4, by successive calls to DAK.

Parameter	Symbol	Description	Dimension	
aerosol model	–	Aerosol model dimension	aer_model	[3]
aerosol subtype	–	Aerosol subtype dimension	aer_subtype	[7]
AOT (354 nm)	$\tau(\lambda_i)$	Aerosol Optical Thickness dimension	aot_354nm	[14]
wavelengths	λ	Wavelength dimension	wavel	[5]
psfc	P_{sfc}	Surface pressure dimension	psfc	[10]
mu_0	μ_0	Solar zenith angle dimension	mu_0	[11]
mu	μ	Viewing zenith angle dimension	mu	[11]
dphi	$\Delta\phi$	Relative azimuth angle dimension	dphi	[19]
dalp	dp_{aer}	Aerosol pressure dimension (p_{sfc}-p_{aer})	dalp	[6]

Table 3: LUT dimensions for the AOT retrieval

Parameter	Symbol	Description	Dimensions
r0	R_0	Path reflectance	wavel, aer_subtype, psfc, dalp, aot_354nm, mu0, mu, dphi
trans	T	Transmission	wavel, aer_subtype, psfc, dalp, aot_354nm, mu0, mu
s_star	s^*	Spherical albedo	wavel, aer_subtype, psfc, dalp, aot_354nm, mu0, mu
alp	p_{aer}	Aerosol layer pressure	wavel, aer_subtype, psfc, dalp, aot_354nm
tau_aer	τ	Aerosol optical thickness	wavel, aer_subtype, psfc, dalp, aot_354nm
tau_gas	τ_{gas}	Gas optical thickness	wavel, aer_subtype, psfc, dalp, aot_354nm
tau_ray	τ_{Ray}	Rayleigh optical thickness	wavel, aer_subtype, psfc, dalp, aot_354nm
tau_tot	τ_{tot}	Total optical thickness	wavel, aer_subtype, psfc, dalp, aot_354nm
ssa	ω_0	Single scattering albedo	wavel, aer_subtype
asym	–	Aerosol asymmetry parameter	wavel, aer_subtype
reff	–	Aerosol effective radius	wavel, aer_subtype

Table 4: RTM LUT parameters

The table has a size of 857 Mb.

6.4 Scene selection

First a selection of scenes is made. Cloud and sun glint contamination are fateful for an accurate AOT retrieval and need to be filtered. Furthermore, ice and snow conditions need to be filtered, together with scenes having extreme viewing and solar zenith angles. The filtering and validity boundaries of the algorithm are described in this section. The configuration parameters determine the behaviour of the algorithm for various circumstances and can be changed for different version of the algorithm without software changes. The configuration of the algorithm described in this ATBD is given in Table 5.

For information on the cloudiness of the scenes the S5P NPP-VIIRS L2 product is used. The S5P NPP-VIIRS product is based on observations performed by the VIIRS instrument onboard the Suomi NPP satellite. The S5P and NPP satellites are kept in a 'loose' formation in very similar orbits, resulting in only a relatively small time difference (currently the difference is approximately 3 minutes, reduced from 5 minutes at the start of the mission). The VIIRS cloud information is provided for each individual TROPOMI footprint, and for three additional sets of boxes surrounding the TROPOMI measurement footprint of increasing size. Using the largest surrounding box for cloud screening assures that also the surroundings of the cloud-free TROPOMI footprint are cloud-free, which can effectively remove cloud shadows and uncertainties in the cloud filter due to the time differences between S5P and NPP.

The S5P NPP-VIIRS cloud product reports for each TROPOMI footprint the number of VIIRS observations which were confidently clear ($N_{\mathrm{c.clr}}$), probably clear ($N_{\mathrm{p.clr}}$), probably cloudy ($N_{\mathrm{p.cld}}$), and confidently cloudy

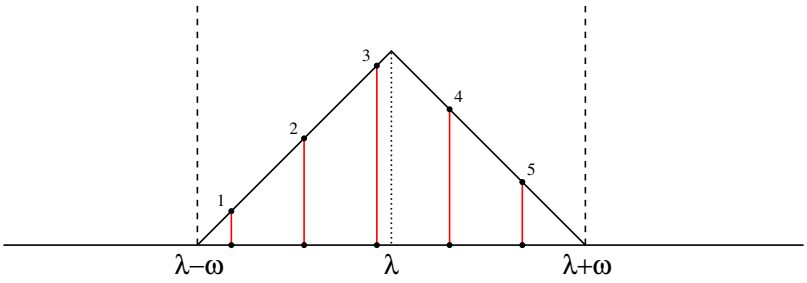

Figure 4: A simple triangular function providing the weighting factors w_i for the detector pixels that lie within the bandwidth 2ω of the wavelength band. w_i are the relative lengths of the red lines.

($N_{\mathrm{c.cld}}$)[RD23]. The respective fields in the S5P NPP-VIIRS product are vcm_confidently_clear, vcm_probably_-clear, vcm_confidently_cloudy, and vcm_probably_cloudy. In these fields, the numbers are reported for four different definitions of (artificial) FOV inside the cloud product [RD23].

The geometric cloud fraction cf for a TROPOMI footprint is defined as the number of (confidently plus probably) cloudy VIIRS observations divided by the total number of VIIRS observations:

$$\mathrm{cf} = \frac{N_{\mathrm{c.cld}} + N_{\mathrm{p.cld}}}{N_{\mathrm{c.clr}} + N_{\mathrm{p.clr}} + N_{\mathrm{c.cld}} + N_{\mathrm{p.cld}}} \tag{13}$$

The cloud fraction found this way provides important information about the amount of cloud cover present in the observed scenes. Cloud-free scenes are selected by filtering those footprints that have a geometric cloud fraction for the exact footprint smaller than CF_max1 and a geometric cloud fraction for the largest surrounding box smaller than CF_max2. The thresholds are given in Table 5.

Over oceans, possible sun glint affected regions are filtered by allowing only sun glint angles that are larger than a threshold sun glint angle Θ_SG_1, where the sun glint angle Θ is

$$\Theta = \cos^{-1}\left[\cos\theta_0\cos\theta + \sin\theta_0\sin\theta\cos\Delta\phi\right]. \tag{14}$$

Parameter	Symbol	Unit	Value	Type
Wavelengths used in the algorithm	λ_i	nm	[354.,388.,416.,440.,494.]	float
Threshold UVAI value over land	UVAI0_land	–	1.0	float
Threshold UVAI value over ocean	UVAI0_ocean	–	1.0	float
Threshold CO column northern hemisphere	CO0_NH	molecules cm^{-2}	$2.0 \cdot 10^{18}$	float
Threshold CO column southern hemisphere	CO0_SH	molecules cm^{-2}	$1.6 \cdot 10^{18}$	float
Maximum solar zenith angle	SZA_0	°	75.	float
Maximum cloud fraction for pixel	CF_max1	–	0.02	float
Maximum cloud fraction for largest surrounding box	CF_max2	–	0.2	float
sun glint scatter angle	Θ_SG_1	°	18.	float

Table 5: Configuration parameters

6.5 Level 1B preparation

In the current set-up the L1B input data are the same as for the LER and directional LER (DLER) computation. The AOT is computed using reflectance measurements in small wavelengths bands for the wavelength mentioned above. The method is outlined below and is the same for the reflectances used in the computation of the DLER. Since the AOT reflectance measurements are a subset of the DLER reflectance measurements, the input from the DLER (in Scene-LER files) is used. Therefore, all information from the DLER ATBD ([AD3]) is also relevant here.

Reflectances are computed using the TROPOMI L1B irradiance and radiance data. In the algorithm, before the band reflectances R_λ are determined for each wavelength band centered around wavelength λ, the solar

irradiance E_0 is first ported to the wavelength grid of the Earth radiance I. The method is described in appendix B of the S5P NO2 ATBD [RD16]. Next, the Earth reflectance R is calculated for all detector pixels using equation 11. Monochromatic reflectances are computed from the spectra by identifying detector pixels that lie within the wavelength ranges $[\lambda - \omega_\lambda, \lambda + \omega_\lambda]$, where $2\omega_\lambda$ is the width of the wavelength band. The wavelength band widths are configurable, but typically 1 nm. The reflectances R of these detector pixels are then averaged, weighted by a triangular function, illustrated graphically in Figure 4. In Figure 4 a total of five detector pixels, indicated with labels i, are weighted with five weighting factors w_i (the relative height of the triangular function indicated in red). Then $R_\lambda = \sum w_i \cdot R_i / \sum w_i$. The triangular function stabilises the band reflectance R_λ, making it less susceptible to detector pixels close to the band edges that are irregularly part of the averaging procedure. This procedure effectively prevents jumps along the across-track direction of the orbit swath.

6.6 Surface reflectivity

The surface reflectivity over land surfaces are computed using the minimum Lambertian Equivalent Reflectivity (LER) from five years of TROPOMI data as available in the TROPOMI DLER surface reflectivity climatology, described in the DLER ATBD. The reflectance for water surfaces are derived using a model based on the Fresnel reflection for a surface with wind-driven waves [RD23] and the ocean colour modelled as a function of the chlorophyll content (Morel and Maritorena, 2001) and foam. This model is used to compute the direct reflectance (for the direct path from the Sun to the satellite), as well as for diffuse isotropic reflectance. The code is described in [AD4].

The TROPOMI surface DLER version 2.1 at a resolution of one month and a $0.125^\circ \times 0.125^\circ$ lat-lon grid is used.

6.7 Aerosol model selection

The algorithm distinguishes three main aerosol types: desert dust, biomass burning and weakly absorbing aerosols. These aerosol models were described in section 6.2.4. Each of the three aerosol types is represented by seven aerosol subtypes of varying single scattering albedo, for a total of twenty-one aerosol models. The micro-physical properties of the twenty-one aerosol models are based on long-term statistics of ground-based observations by the Aerosol Robotic Network (AERONET).

The aerosol type selection is based on the TROPOMI UVAI, the TROPOMI CO total column and the surface type and is shown in Figure 5. It uses thresholds for UVAI and CO columns. Note that all the numbers that are used should be configurable. A different threshold is used for the Northern (CO0_NH) and Southern hemisphere (CO0_SH). A simple linear interpolation between 10°S to 10°N is used to make a smooth transition.

The UVAI is derived from the same wavelength bands as used for the AOT algorithm and is therefore by definition aligned.

6.8 Aerosol Layer Height

Aerosol Layer Height (ALH) is currently computed from the CAMS 2003-2013 Control Run climatology [RD24]. This climatology provides 4D distributions of biomass burning aerosols, dust, organic aerosol and sea salt, at a grid of 12 months, 60 vertical levels and $1^\circ \times 1^\circ$ lat, lon. The aerosol layer height is defined as the height at which the mass concentration becomes $1/e$ of the total column mass concentration, at each grid cell. Examples for different aerosol models are shown in Fig. 6. Note that the aerosol scale height is expressed in pressure in hPa, and that only scale heights are plotted when total mass concentrations are larger than $1{\cdot}10^{-5}$ kg m^{-2}. This is comparable to the figures in Appendix A of [RD24].

The TROPOMI Aerosol Layer Height AER_LH product is available globally since version 2.2.0 of the TROPOMI L2 data was released (July 2021). The current version 2.6.0 of the AER_LH has been improved to include the surface albedo in the optimal estimation feature vector, with the purpose of improving the ALH retrievals over land, which up till the current version were biased towards the surface. If the TROPOMI AER_LH L2 product shows a compliance with the GCOS requirements in all cases (i.e. over land and ocean surfaces), the CAMS ALH may be replaced by the TROPOMI AER_LH in the AOT algorithm. However, in the current set-up CAMS is used and the TROPOMI L2 AER_LH is present as an output field of the AOT product for future use. The TROPOMI L2 AER_LH, derived from the NIR channel, is interpolated to the UVVIS channel using nearest-neighbour interpolation.

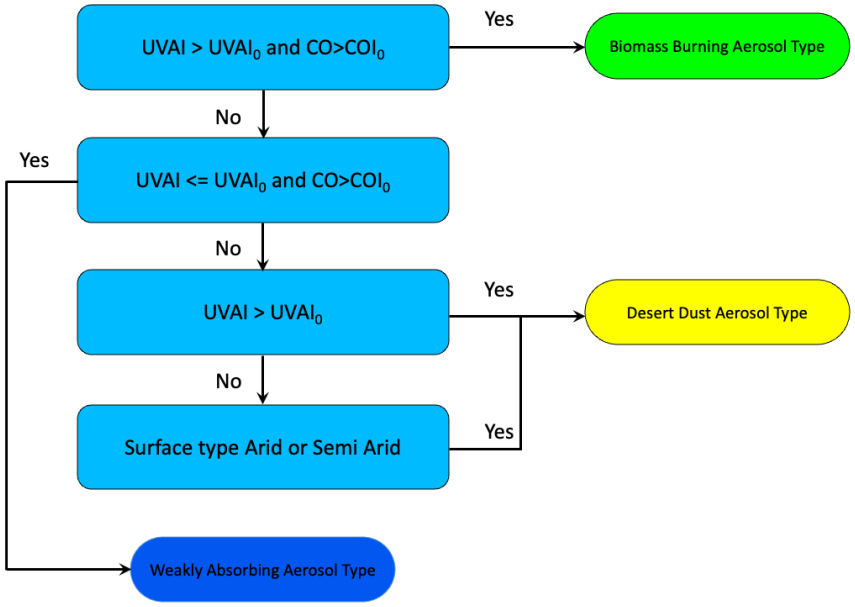

Figure 5: Aerosol model selection flow chart

6.9 Computation of the AOT and SSA

This module computes the AOT and SSA based on the L1B input and RTM LUTs. It matches the measured reflectance by interpolation of the LUT, using the selected aerosol type. First, for each pixel, the LUT reflectance for the selected aerosol type is interpolated for the given geometry $(\mu, \mu_0, \phi, \phi_0)$ and the layer height, giving the simulated reflectance as a function of the wavelength, aerosol subtype and aerosol optical thickness.

6.9.1 Aerosol sub-type computation

The aerosol subtype can be found as a function of the aerosol reflectance. The aerosol reflectance is determined from the measured reflectance subtracted with the modelled aerosol-free reflectance computed using the LUT reflectance. This was determined above as a function of aerosol optical thickness, so the aerosol-free reflectance is the node with AOT=0. The subtype can discriminated using the aerosol reflectance at 388 nm and the difference in the reflectance at 354 and 388 nm [RD25]. The procedure was illustrated in Figure 3b. Here, a possible measurement is indicated by the red lines. To determine the aerosol subtype a two-dimensional interpolation using radial base functions is performed. The interpolation returns the aerosol subtype as a floating-point number between 1 and 7.

6.9.2 Interpolation to AOT and SSA

Once the aerosol subtype is known, the AOT and SSA can be computed. First, the aerosol reflectance and the single scattering albedo for the derived aerosol subtype are linearly interpolated. Next, the AOT is computed using piecewise linear interpolation of the AOT as a function of the aerosol reflectance. The AAOT can be found as the product of the aerosol optical thickness and the single scattering albedo.

6.9.3 Precision of the Aerosol optical thickness

The aerosol optical thickness precision is not computed from the reflectance precision, because the SNR is high for TROPOMI and the reflectance precision does not reflect the uncertainty of the derived AOT. Error sources like the model selection and the surface albedo determine the uncertainty of the derived AOT. Instead. the precision is determined from the prelimiary validation study of the TROPOMI AOT using 31 AERONET stations, as described in [AD5]. The precision is computed as $d\sigma = 0.13 + 0.58 \cdot \sigma$.

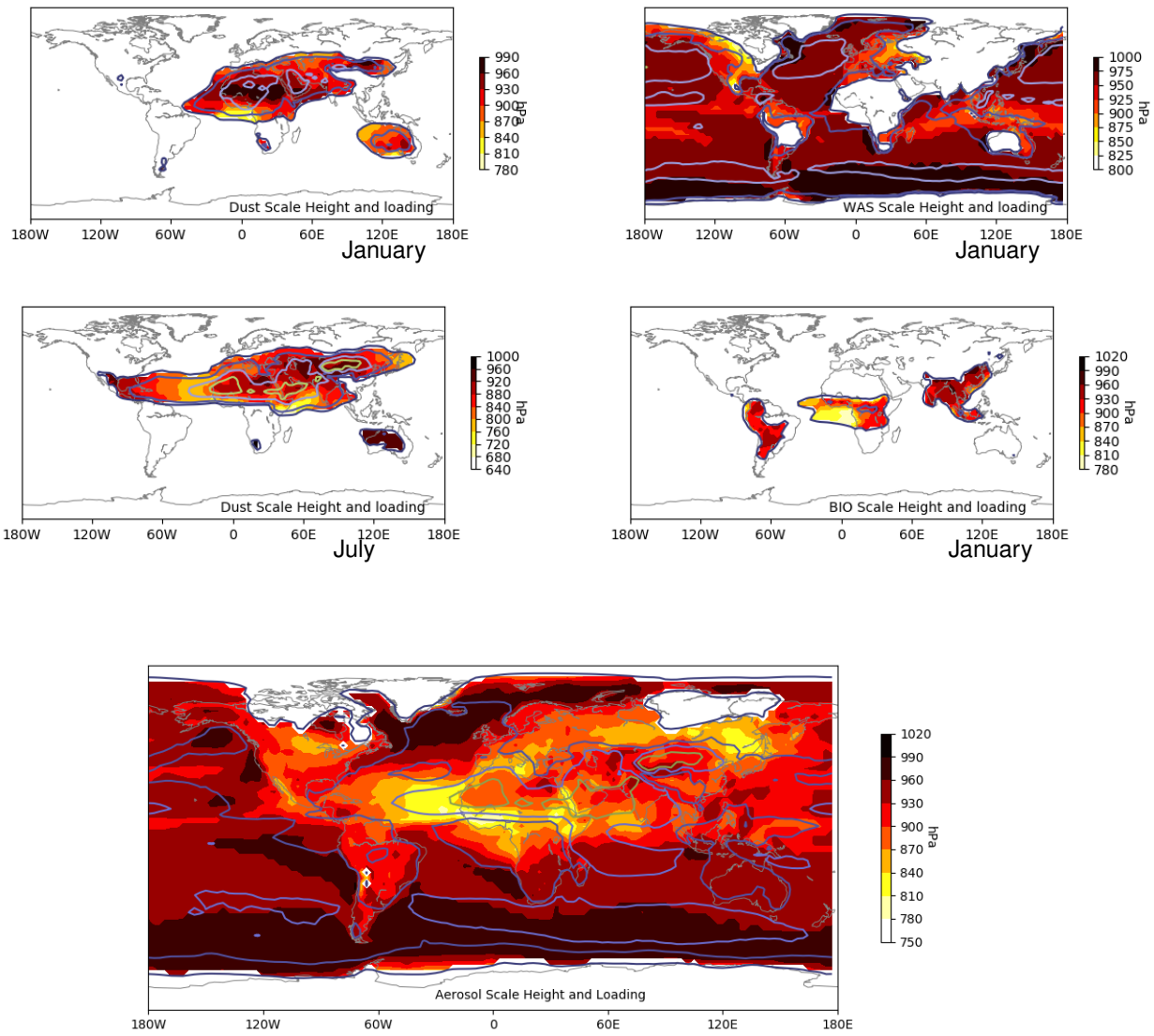

Figure 6: Scale height (plotted as the pressure in hPa as coloured shades) and aerosol loading (in contour lines of 0,1·10^{-5}, 5·10^{-5}, 1·10^{-4}, 3·10^{-4}, 8·10^{-4} kg m^{-2}) for three aerosol models (DST, WAS, BIO) and all aerosol models together from the CAMS control run over the years 2003–2013. Note that the scale height is only plotted for aerosol loadings $>$ 1·10^{-5} kg m^{-2}. All shown plots are for the month January, except for Dust, which is the only aerosol model to show a strong annual cycle, and is also shown for July.

7 Feasibility

7.1 Computational Effort

The AOT retrieval is a 'classic' retrieval, in the sense that one retrieval is performed per selected ground pixel. This means that the computational effort scales linearly with the number of selected pixels, which in this case is the number of cloud-free pixels. It also means that the processing can easily be parallelized.

In order to estimate the computational effort, the computation time of the AOT algorithm was tested by processing one day of TROPOMI data on a workstation using a single core. Processing 14 orbits on this system took 105 hours, which amounts to 7.5 hours per orbit. The workstation specification were as follows:

System: Dell
CPU: Intel® Core™ i7-9700 (3.00GHz)
Memory: 32 GB memory
OS: Fedora 33 Workstation
Kernel: 5.12.7-200.fc33.x86_64

A more operational-like environment is available on the S5P Product Algorithm Laboratory (PAL). To estimate the processing effort for parallel processing on multiple cores, the processing time for processing the AOT in 2019 on PAL was estimated. 50 cores were available for processing, and processing two months worth of data, which is about 840 orbits, took about 63 hours. This means an average processing time per orbit of 50 $\times$ 4.5 minutes, or 225 minutes (3.75 hours).

In general, the processing of a single orbit varied between about 1.5 hours and 6 hours.

7.2 Dynamic input

The dynamic input for the aerosol optical thickness algorithm is listed in Table 6.

Parameter	Symbol	Unit	Source	Use	If unavailable
Irradiance	E_0	$\frac{\text{mol}\cdot\text{s}^{-1}\text{m}^{-2}}{\text{nm}^{-1}}$	S5P L1B	U	Use previous day
Radiance	I	$\frac{\text{mol}\cdot\text{s}^{-1}\text{m}^{-2}}{\text{nm}^{-1}\text{sr}^{-1}}$	S5P L1B	U	No processing
Irradiance noise	δE_0	$\frac{\text{mol}\cdot\text{s}^{-1}\text{m}^{-2}}{\text{nm}^{-1}}$	S5P L1B	U	Use previous day
Radiance noise	δI	$\frac{\text{mol}\cdot\text{s}^{-1}\text{m}^{-2}}{\text{nm}^{-1}\text{sr}^{-1}}$	S5P L1B	U	No processing
Irradiance wavelength	λ_{E_0}	nm	S5P L1B	U	No processing
Radiance wavelength	λ_I	nm	S5P L1B	U	No processing
cloud fraction	cf	-	S5P L2 VIIRS cloud	F	No processing
Ground pixel	i		S5P L1B	U	No processing
Ground pixel quality	-	-	S5P L1B	F	climatology
Aerosol absorbing index	AAI	-	S5P L2 AAI	U	No processing
Aerosol layer pressure	ALH	hPa	CAMS	U	No processing
Temperature profile	$T(p_i)$	K	S5P L2 ALH	U	climatology
Pressure profile	$p(z)$	hPa	S5P L2 ALH	U	climatology
Surface pressure	p_s	hPa	S5P L2 ALH	U	1013 hPa scaled by altitude DEM
Surface albedo	A_s	-	S5P L3 DLER	U	OMI LER
CO total column	CO	mol m^{-2}	S5P L2 CO	U	No processing
Ozone total column	Ω	mol m^{-2}	S5P L2 O3	U	No processing
Chlorophyll concentration	chl	mg m^{-2}	Ocean GLOB product	U	fixed ocean surface albedo
Windspeed	|U|	m s^{-1}	S5P L2 AAI	U	fixed ocean surface albedo

Parameter	Symbol	Unit	Source	Use	If unavailable
snow_ice_flag	f_{i}	$--$	NISE	U	No processing
surface_classification		–	S5P L3 DLER	U	No processing
Latitude	lat	$^\circ$	S5P L1B	C	No processing
Longitude	lon	$^\circ$	S5P L1B	C	No processing
Solar zenith angle	θ_0	$^\circ$	S5P L1B	U	No processing
Solar azimuth angle	ϕ_0	$^\circ$	S5P L1B	U	No processing
Viewing zenith angle	θ	$^\circ$	S5P L1B	U	No processing
Viewing azimuth angle	ϕ	$^\circ$	S5P L1B	U	No processing
		U=Used in computation; F=Filter; C=Copied to output only.			

Table 6: Dynamic input for the Aerosol Optical Thickness retrieval algorithm

7.3 Static input

The static input for the Aerosol Layer Height algorithm is listed in Table 7.

Parameter	Symbol	Unit	Source	Use	If unavailable
Minimum/Mode/Directional LER climatology	$\mathrm{LER}_{\mathrm{min}}(t,\lambda)$	–	S5P L3 DLER	U	OMI LER
Reflectance	$\mathrm{LUT}_{\mathrm{R}}$		RTM_LUT file	U	No processing
Aerosol model	$\mathrm{LUT}_{\mathrm{aer}}$		RTM_LUT file	U	No processing

Table 7: Static input for the Aerosol Optical Thickness retrieval algorithm

7.4 Output Product Overview

The Level 2 product format is described in Table 8.

Parameter	Symbol	Unit	Dimensions	Comments
PRODUCT				
time	t	s	time	Reference time [since epoch] of the measurements
time_UTC	t	s	scanline	Time of observation as ISO 8601 date-time string
delta_time	δs	ms	scanline	Time difference with reference time for each scanline
corner		1	4	Pixel corner indices
scanline		1	scanline	Coordinate variable defining the indices along track
ground_pixel		1	ground_pixel	Coordinate variable defining the indices across track
wavelength	λ	nm	wavelength	Baseline wavelengths
aerosol_optical_thickness	τ	–	scanline, ground_pixel, wavelength	Aerosol optical thickness for baseline wavelengths
aerosol_optical_thickness _precision	σ_τ	–	scanline, ground_pixel, wavelength	Precision of the aerosol optical thickness
aerosol_type	–	–	scanline, ground_pixel	Selected aerosol type
aerosol_subtype	–	–	scanline, ground_pixel	Aerosol subtype
latitude		$^\circ$ north	scanline, ground_pixel	Latitude of the center of each ground pixel on the WGS84 reference ellipsoid
longitude		$^\circ$ east	scanline, ground_pixel	Longitude of the center of each ground pixel on the WGS84 reference ellipsoid
qa_value	qa	–	scanline, ground_pixel	Quality assurance value
DETAILED RESULTS				

single_scattering_albedo	ω_0	–	scanline, ground_pixel, wavelength	Single scattering albedo for baseline wavelengths
aerosol_mean_height	z_{mean}	m	scanline, ground_pixel	Mean aerosol layer height
aerosol_reflectance	R_{aer}	–	scanline, ground_pixel, wavelength	Aerosol reflectance
surface_reflectance_diffuse	A_s^{diff}	–	scanline, ground_pixel, wavelength	Diffsue component of the surface reflectance
surface_reflectance_direct	A_s^{dir}	–	scanline, ground_pixel, wavelength	Direct component of the surface reflectance
GEOLOCATION				
geolocation_flags	f	–	scanline, ground_pixel	Geolocation flags
latitude_bounds		° north	scanline, ground_pixel, corner	Latitude of the ground pixel corners
longitude_bounds		° east	scanline, ground_pixel, corner	Longitude of the ground pixel corners
satellite_latitude		° north	scanline	Latitude of the spacecraft sub-satellite point on the WGS84 reference ellipsoid
satellite_longitude		° east	scanline	Longitude of the spacecraft sub-satellite point on the WGS84 reference ellipsoid
satellite_altitude		m	scanline	Altitude of the spacecraft relative to the WGS84 reference ellipsoid
satellite_orbit_phase		–	scanline	Relative offset of the measurement in the orbit
solar_zenith_angle	θ_0	°	scanline, ground_pixel	Solar zenith angle of the ground pixel center
solar_azimuth_angle	ϕ_0	°	scanline, ground_pixel	Solar azimuth angle of the ground pixel center
viewing_zenith_angle	θ	°	scanline, ground_pixel	Viewing zenith angle of the ground pixel center
viewing_azimuth_angle	ϕ	°	scanline, ground_pixel	Viewing azimuth angle of the ground pixel center

Table 8: Level 2 product format

8 Error Analysis

In this section a general description of the expected errors is given.

8.1 Cloud contamination

The most important error source for aerosol optical thickness retrieval is cloud contamination. Even though cloud filters are present to select only cloud-free scenes, the presence of spurious sub-pixel clouds have a large impact on the AOT retrieval, since the optical thickness of clouds is generally so much larger than those of aerosols. Furthermore, clouds and aerosols are difficult to distinguish. If 5% of a pixel contains clouds, the error in the AOT is estimated to be about 0.1 to 0.2 [RD25].

8.2 Surface reflectivity

The surface reflectivity is an important aspect in the retrieval of AOT. For a bright surface the TOA reflectivity can be dominated by the surface signals, and AOT will be difficult to retrieve. This is more pronounced at visible wavelengths than UV wavelengths, where the surface contribution is significantly smaller.

The sensitivity of the TOA reflectance to the surface albedo can be calculated from equation 12 by differentiation, yielding

$$\frac{dR}{dA} = \frac{T}{(1 - A_s s^*)^2}, \tag{15}$$

where A_s the surface albedo, $T = t(\mu)t(\mu_0)$, where t is the total atmospheric transmission, and s^* is the spherical albedo of the atmosphere for illumination from below, as before. This is strongly wavelength-dependent, the surface albedo have almost no effect on the TOA reflectivity in the UV, while for longer wavelengths the effect of the surface albedo increases quickly. In [AD3], Figure 14, the reciprocal effect is plotted, i.e. the spectral dependence of dA/dR, showing the strong wavelength dependence.

8.3 Instrument errors

The AOT is affected by instrumental errors like radiometric calibration offsets, radiometric calibration scale factors and radiometric noise. The L1B data preparation and error propagation are handled by the Scene LER algorithm, and the L2 AOT product is computed from that. Following that, the error in the Earth radiance and solar irradiance are assumed to be independent and the error in the measured Earth reflectance is

$$\delta R = R\sqrt{(\delta I/I^2) + (\delta E_0/E_0)^2} \tag{16}$$

where R is the reflectance, I is the radiance, E_0 is the solar irradiance, and δI and δE_0 are the precisions of the radiance and the solar irradiance, respectively.

8.4 Aerosol models

The algorithm relies heavily on the correct representation of the ambient aerosol by an appropriate aerosol model. In section 6.2.4 the available aerosol models are described, which vary in size distribution, refractive index and vertical profile. It is very important that the aerosol models cover the variations in the atmosphere, and that the correct model is chosen under all circumstances.

The validation tests showed that the largest differences with AERONET measurements of AOT were caused by a wrong representation of aerosol type. With a correct representation of aerosol type, the AOT retrieval was accurate (within the requirements) for more than 80% of the measurements. For cases where inappropriate models were not available or not selected, the accuracy dropped to less than 30%. More information is available in [AD5].

8.5 Aerosol height

A minor contribution to the error budget of AOT is caused by a possible incorrect assumption of aerosol height. In the current set-up a scale height is computed from three aerosol types in the CAMS aerosol distribution climatology, see section 6.8. Since the introduction of TROPOMI version 2.2 L2 algorithms, this may be replaced by the TROPOMI ALH product. However, the contribution of aerosol layer height to AOT is small, and the scale height climatology produces fine results.

9 Validation

A complete validation of the AOT and SSA products is described in [AD5].

The TROPOMI AOT and derived SSA products were validated using ground-based and satellite data. For the ground-based validation AERONET stations at varying locations around the globe were used, to ensure that all common types of aerosols were represented in the comparisons. TROPOMI AOT and SSA data from various sources and at different times were used. Some scientifically produced intermediate data were produced early in the development of the algorithm, to benefit from the lock-down regulations in early 2020 in Italy, which showed severe restrictions for industry and traffic, which was expected to be reflected in the aerosol distributions. Furthermore, data were processed on the newly developed PAL environment, which allows the algorithm developer to process data at an almost operational level. Two months worth of data from this platform were used to compare global data with AERONET stations. No differences were found between the PAL-produced product and the scientific data.

Comparisons of AOT from TROPOMI with AERONET data showed good comparisons, with the majority of the data being within the requirements. For most stations the fraction of data falling within the requirements was higher than 80%. For a few stations this dropped below 60% to less than 30% of AOT measurements within the requirements for one station. The main reason for the lower correlations is the selection of aerosol type, for which the algorithm is very sensitive. With an inappropriate aerosol model the algorithm will not be able to retrieve an accurate AOT.

A comparison of AOT from TROPOMI with collocated VIIRS AOD measurements did not show a good correlation, even though S5P and Suomi-NPP fly in synchrony and the collocation is almost perfect. Both algorithms have their own aerosol model selection strategy, and this results in rather large differences between the products. The intrinsic properties of aerosols are important in the inversion schemes, and if one or either model is incorrect the retrieval will fail to give consistent results.

The previous problem is most palpable in the SSA comparison. No correlation was found between the SSA from TROPOMI compared to AERONET. Even though the AOT compared reasonably well, the SSA shows no skill. This is in accordance with other satellite SSA and AAOT products, which currently show no to very low skill. This problem should be resolved using satellite missions dedicated to retrievals of aerosol properties and algorithms that are able to utilize all the information in the measurements of these missions. Examples are upcoming satellite missions like 3MI and EarthCare, and algorithms like GRASP.

10 Conclusion

This document describes the AOT and SSA retrieval algorithm for S5-Precursor/TROPOMI. The algorithm was tested and validated. The algorithm is described in the current document. Validation results are available in [AD5]. A complete product description, including the input/output specifications, metadata, quality assurance parameters and flags is available in [AD5]. The product is available on the PAL platform [ER2] provided by ESA.